Article

Calculation of Characteristic Point Parameters for Restoring Model of Corroded Short-Pier RC Shear Walls

Qing Qin [1,2,*], Haojie Cheng [1], Chenghua Zhang [1] and Sha Ding [3]

1   School of Civil and Architecture Engineering, Xi'an University of Science and Technology,
    Xi'an 710054, China; 22204228080@stu.xust.edu.cn (H.C.)
2   State Key Laboratory of Green Building in Western China, Xi'an University of Architecture & Technology,
    Xi'an 710055, China
3   Department of Civil Engineering, Xi'an University of Architecture and Technology, Xi'an 710055, China;
    dingsha1989@xauat.edu.cn
*   Correspondence: qinqing@xust.edu.cn

Abstract: Based on the quasi-static tests of 12 corroded RC (reinforced concrete) shear walls, it was found that reinforcement corrosion has a great influence on the skeleton curve of RC shear walls. With an increase in the degree of corrosion, the bearing capacity of specimens decreases, and the deformation capacity worsens. Increasing the diameter of longitudinal reinforcements can significantly improve the bearing capacity of corroded RC shear walls, while the deformation capacity of corroded specimens can be improved by increasing the lateral distributed reinforcement or the transverse reinforcement in the embedded column. In order to accurately evaluate the seismic performance of corroded RC shear walls, we considered descent segments of four broken-line models to estimate the skeleton curve. After considering the influence of corrosion on the parameters of the characteristic point for the skeleton curve, the calculation formulas of the characteristic point parameters of the skeleton curve for the corroded RC shear wall were determined based on the test data fitting. It was proven that the formula for the characteristic point parameters for the skeleton curve of corroded RC shear walls has good applicability. This study lays a theoretical foundation for the seismic performance evaluation of an RC shear wall structure in a salt fog environment. It provides a theoretical basis for further improving the life-cycle seismic capacity evaluation system for RC structures.

Keywords: RC shear wall; corrosion; pseudo-static test; characteristic point for skeleton curve

1. Introduction

In a marine environment (splash area, salt fog area, and tidal area) and deicing salt environment, the main load-bearing components of existing reinforced concrete buildings are cracked to varying degrees, which is mainly caused by chloride ion erosion of reinforcement [1]. RC shear walls are widely used in practical engineering because of their large lateral stiffness and high bearing capacity. For high-rise buildings in coastal areas and underground garages, RC shear wall components are vulnerable to corrosion by salt fog and deicing salt chloride, as reported in [2]. With an increase in the service age of structures, the continuous accumulation of corrosion leads to the degradation of the mechanical properties of RC shear walls, which reduces the overall seismic performance of the structures.

Many experiments by Mahadik et al. [3,4], have studied the seismic performance of intact RC shear walls, while there are relatively few studies on corroded RC shear walls. Yamakawa T. [5] corroded two squat RC shear walls with the galvanizing method and then carried out a pseudo-static loading test (low-frequency cyclic loading test). The results indicate that steel corrosion has a significant impact on the seismic performance of shear walls. Zhuang Y. [6] studied the seismic capacity of squat RC shear walls with different

surface covering materials after corrosion, establishing a mechanical model to evaluate the seismic performance of corroded buildings. Zheng S. et al. [7] and Zheng Y. et al. [8] used the artificial climate simulation method to accelerate the corrosion of squat RC shear walls, focusing on the restoring force characteristics of corroded components. The results indicate that the artificial climate accelerated corrosion method causes pitting corrosion of steel bars, which is similar to the actual corrosion environment. Shen D. et al. [9] and Li M. et al. [10] used the electrochemical corrosion method to accelerate corrosion of shear walls, focusing on the seismic performance of corroded specimens and BFRP (basalt fiber-reinforced polymer)-repaired specimens. Yang L. et al. [11] and Liu X. et al. [12] studied the seismic performance of corroded T-shaped shear walls and considered the effects of axial compression ratio and corrosion rate. The above studies qualitatively evaluated the seismic performance of corroded RC shear walls but did not quantitatively analyze its degradation degree.

The simplified restoring force model can facilitate evaluation of the seismic performance of concrete components. The restoring force model is a mathematical model established based on regression and theoretical analysis of a large amount of experimental data. This model can accurately reflect the macroscopic dynamic characteristics of a structure through the analysis of elastic-plastic seismic response. Nowadays, there are many formulas for calculating the characteristic points parameters of an intact RC shear wall skeleton curve but few reports on corroded RC shear walls. In this paper, four broken-line models that consider the descent segment are adopted to estimate the skeleton curve. Furthermore, the relationship between the reduction coefficient of characteristic point parameters and the degree of corrosion is obtained by fitting the test data of corroded specimens; these data are based on the calculation formula of characteristic point parameters for intact RC shear walls. Finally, we established a calculation formula with good applicability for characteristic points of RC shear wall skeleton curves; this formula takes into account reinforcement corrosion. Calculation of characteristic point parameters for a restoring model of corroded short-pier RC shear walls of various ages can quickly evaluate the seismic performance of concrete components in harsh environments.

2. Skeleton Curves of Corroded RC Shear Walls Test

2.1. Test Description

In this paper, artificial climate environment simulation technology was used to simulate the offshore atmospheric environment to accelerate the corrosion of 12 RC shear walls with a shear span ratio of 2.14. After reaching the expected corrosion target, a pseudo-static loading test was carried out. All specimens were made of C30 fine aggregate concrete, and the thickness of the protective layer of the wall panel was 10 mm. For the walls, the mix proportion of the concrete was 320 kg/m^3 of P.O32.5R cement, 870 kg/m^3 of medium sand, 870 kg/m^3 of fine stone, 135 kg/m^3 of water, 11.07 kg/m^3 of water-reducing admixture, and 90 kg/m^3 of fly ash. The longitudinal reinforcements of the concealed columns were made of HRB335; its yield strength was between 310 MPa and 350 MPa, as measured through tensile tests. Simultaneously, the stirrups of the concealed columns and the distribution reinforcements of the walls were made of HPB235, the yield strength of which was 305 MPa. The detailed design parameters of the specimens are shown in Table 1, and the geometric dimensions and detailed reinforcements of the specimens are shown in Figure 1.

Table 1. RC shear wall design parameters.

Specimen No.	Axial Compression Ratio	Transversely Distributed Reinforcement	Longitudinal Reinforcement of Concealed Column	Concealed Column Stirrup	Design Corrosion Crack Width	Flexural Shear Ratio
SW-1	0.1	A6@200	4B12	A6@150	0.8 mm	0.938
SW-2	0.2	A6@200	4B12	A6@150	0 mm	1.002

Table 1. *Cont.*

Specimen No.	Axial Compression Ratio	Transversely Distributed Reinforcement	Longitudinal Reinforcement of Concealed Column	Concealed Column Stirrup	Design Corrosion Crack Width	Flexural Shear Ratio
SW-3	0.2	A6@200	4B12	A6@150	0.3 mm	1.002
SW-4	0.2	A6@200	4B12	A6@150	0.8 mm	1.002
SW-5	0.2	A6@200	4B12	A6@150	1.2 mm	1.002
SW-6	0.2	A6@150	4B12	A6@150	0.8 mm	0.874
SW-7	0.2	A6@100	4B12	A6@150	0.8 mm	0.695
SW-8	0.2	A6@200	4B14	A6@150	0.8 mm	1.196
SW-9	0.2	A6@200	4B8	A6@150	0.8 mm	0.703
SW-10	0.2	A6@200	4B12	A6@100	0.8 mm	1.002
SW-11	0.2	A6@200	4B12	A6@200	0.8 mm	1.002
SW-12	0.3	A6@200	4B12	A6@150	0.8 mm	1.002

Note: the axial compression ratio n in this paper refers to the test axial compression ratio, which is calculated according to $n = N/(f_c A)$, where f_c is the average value of axial compressive strength of concrete, N is the vertical axial force of the wall, and A is the cross-sectional area of the wall. The flexural shear ratio m refers to the ratio of flexural capacity M_u and shear capacity V_u calculated according to the actual reinforcement of shear wall specimens, which is calculated according to $m = M_u/(V_u H)$, where M_u and V_u can be calculated according to relevant formulas in [13], and H is the height of the wall.
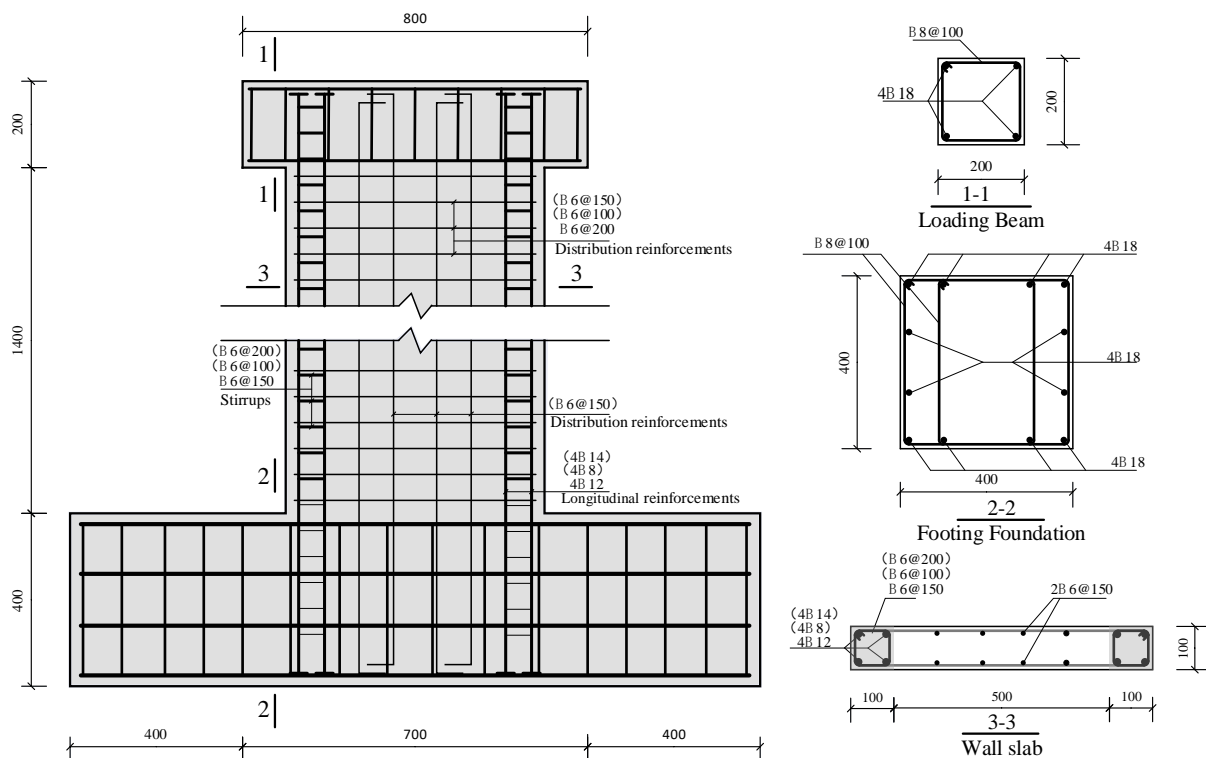

Figure 1. Geometric size and reinforcement detail drawings.

In the test, 5% NaCl liquor was mainly used to form salt spray through the "nozzle" of the salt spray device, and a dry–wet cycle was used to improve the chloride ion erosion rate. First, the temperature in the test chamber was raised to 45 °C, the humidity RH was set at 90%, and intermittent spray was used to keep the salt spray concentration in the salt spray chamber constant. The spray lasted for 20 min, and the intermission lasted for 40 min; the procedure lasted for 3 h in total. Subsequently, the test chamber was heated to 60 °C for drying for a total of 2 h. Finally, in the test chamber, fresh water was sprayed for 3 min to clean the crystal salt of the nozzle and ensure normal execution of the salt spray test. It was determined that completing a simulation dry–wet cycle required a total of 6 h (including

time for heating and cooling). The corrosion degree of the specimen was controlled by the width of the rust expansion crack, which was same as the Ref. [14]. Subsequently, we entered the test chamber regularly, and a ZBL-F130 crack observer (accuracy 0.01 mm, range 0~10 mm) was used to measure the transverse and longitudinal crack width within the plastic-hinge height (700 mm) of the test piece. When the larger of the two mean values reached the design rust expansion crack width in Table 1, the test pieces were taken out of the test chamber in batches. Finally, the bottom beam and top beam of the specimen were poured twice, and the mixed load-displacement mode was used for loading. The exposed steel bars were sealed during the corrosion process with wrapped plastic film and epoxy resin to prevent corrosion. The test process is shown in Figure 2.
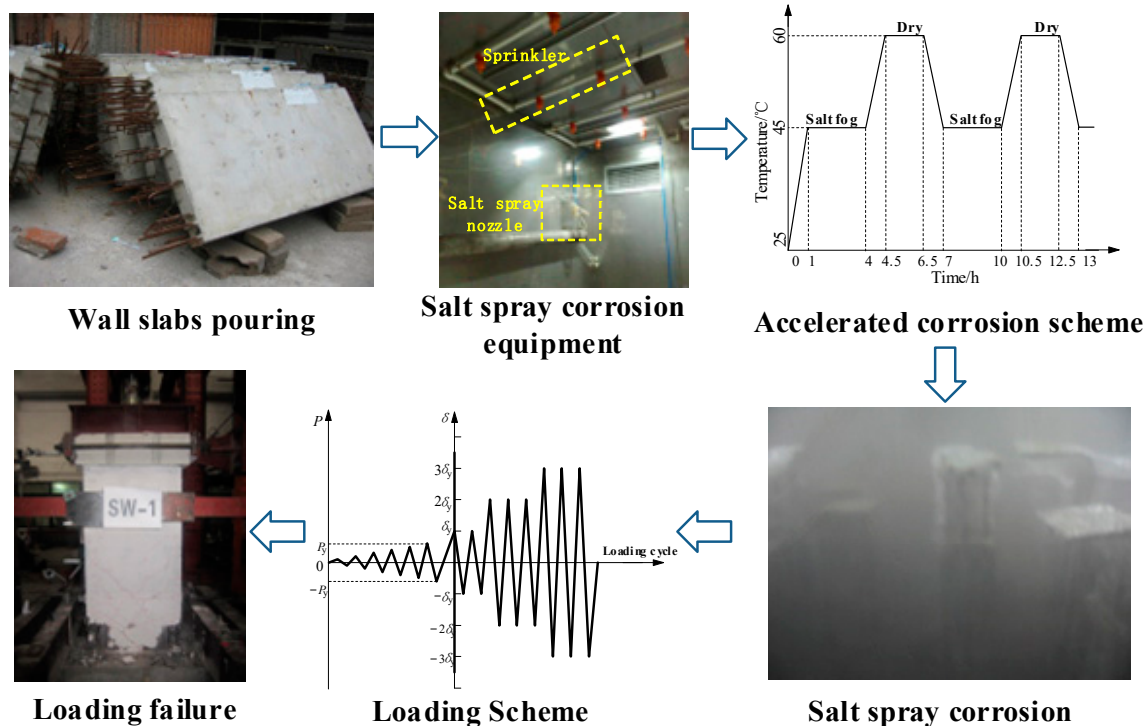

Wall slabs pouring

Salt spray corrosion equipment

Accelerated corrosion scheme

Loading failure

Loading Scheme

Salt spray corrosion

Figure 2. Test flow.

2.2. Corrosion Phenomenon

(1)　Rust expansion crack width

　　Under the action of rust expansion force, cracks were produced along the reinforcement in the concrete protective layer of the shear wall specimen, as shown in Figure 3.

　　It can be seen from the figure that the width of the rust expansion cracks along the longitudinal reinforcements of the concealed column were wider and developed along the full length of the column, while the width of the rust expansion cracks in the distribution reinforcements and stirrups was smaller, and, in the latter, the radial micro-cracks were generated in the direction of the reinforcements. The initial corrosion rate required to cause concrete rust expansion cracking was directly proportional to the thickness c of the concrete cover and inversely proportional to the diameter d of the reinforcement. Since the c/d value of the longitudinal reinforcement (1.33) was less than that of the stirrup and distribution reinforcement (1.67), rust expansion cracks along the longitudinal reinforcement appeared earlier, resulting in a large crack width, as shown in Figure 3. In addition, due to less corrosion products produced by the distribution reinforcements and stirrups with large spacing, the width of the rust expansion cracks along the distribution reinforcements and stirrups were smaller: roughly in the range of 0.2~0.4 mm. The number of radial micro-cracks continued to increase with the increase in corrosion time, as shown in Figure 3.

SW-3(Crack width unit: mm)

SW-4(Crack width unit: mm)

(**a**)   (**b**)   (**c**)
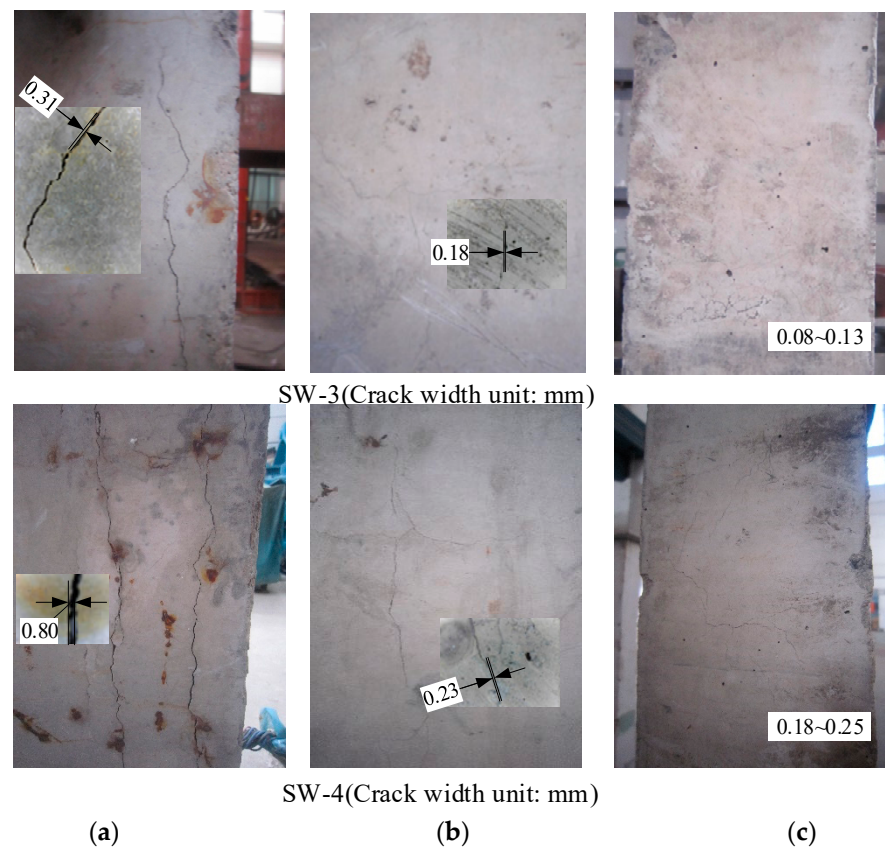
Figure 3. Rust expansion crack of concrete cover. (**a**) Longitudinal cracks; (**b**) horizontal cracks; (**c**) lateral cracks.

(2)   Corrosion rate of reinforcement

In order to further understand the internal reinforcement corrosion of the specimens, after a loading test was completed, a breaking test was carried out on the shear wall specimen. Six longitudinal bars (200 mm), stirrups (300 mm), and distribution bars (400 mm) of the same length were cut at different positions in the 700 mm area of the wall bottom for observation. It was found that the corrosion degree of the reinforcement became more and more serious with the increase in the rust expansion crack width, the black-brown corrosion products increased, the cross-sectional area of reinforcement decreased, and the surface pit corrosion phenomenon became more and more obvious. These findings were different from the uniform corrosion phenomenon observed in general electrochemical corrosion. On the contrary, these finding were more consistent with the corrosion phenomenon in the actual environment. The average corrosion rate ρ for different types of reinforcement for each specimen is shown in Table 2.

Table 2. Corrosion degree of specimens.

| Specimen No.	Distributed Reinforcement $\rho_{d,average}$/%	Stirrup $\rho_{s,average}$/%	Longitudinal Reinforcement $\rho_{l,average}$/%	Average Width of Rust Expansion Crack/mm
SW-1	19.36	16.33	5.31	0.78
SW-2	0	0	0	0
SW-3	8.55	7.87	2.24	0.29
SW-4	18.73	17.13	5.63	0.81
SW-5	23.37	24.39	8.42	1.18

Table 2. *Cont.*

Specimen No.	Distributed Reinforcement $\rho_{d,average}$/%	Stirrup $\rho_{s,average}$/%	Longitudinal Reinforcement $\rho_{l,average}$/%	Average Width of Rust Expansion Crack/mm
SW-6	20.66	16.69	5.33	0.77
SW-7	17.38	15.12	5.51	0.79
SW-8	18.54	17.05	4.38	0.83
SW-9	20.13	18.47	6.25	0.77
SW-10	19.87	18.19	5.92	0.77
SW-11	18.17	16.88	4.86	0.82
SW-12	16.33	15.22	5.27	0.78

2.3. Discussion of Skeleton Curves

In this study, corrosion of reinforcements reduced the cross-sectional area of stressed reinforcements, and corrosion products reduced the bonding force of concrete. On the other hand, the corrosion of reinforcements led to rust expansion cracks in the concrete protective layer along the reinforcement. Therefore, reinforcement corrosion had a great impact on the loading failure process, hysteretic curve, skeleton curve, strength, stiffness, and energy consumption of RC shear wall. This paper focuses on the impact of corrosion reinforcement on the skeleton curves of RC shear walls. Figure 4 was created using the method specified in [15]. As can be seen in the figure, before cracking, the skeleton curve of each specimen basically remained linear, and the slope was approximately the same, indicating that different corrosion degrees and different design parameters had little effect on the initial stiffness of corroded specimens. With a further increase in load, the skeleton curve gradually deviated from a straight line, demonstrating the characteristics of elastic-plastic deformation. At this time, the corrosion degree and design parameters had a great impact on the skeleton curve of the corroded specimen, mainly as follows:

(1) With the increase in the width of the rust expansion crack, the longitudinal reinforcement and distribution reinforcement of the specimen were corroded more and more seriously, the bearing capacity of the specimen decreased continuously, and the deformation capacity became worse, but it still had high bearing capacity and deformation capacity. The main reason for this was that the rust expansion crack mainly caused the cracking of the protective layer of the concealed column along the longitudinal reinforcement of the specimen, and the impact of corrosion and protective layer cracking on the bearing and deformation capacity was limited. This was consistent with the references [2] described, as shown in Figure 4a;

(2) With a decrease in the spacing of the transverse distribution bars, the bearing capacity of the corroded specimens did not increase significantly, which mainly improved the deformation capacity of the specimens. The main reason for this was that reducing the spacing of the distribution bars improved the shear capacity of the corroded specimens and gradually changed the specimens from demonstrating bending shear failure to demonstrating bending failure, which was consistent with the references [8] described, as shown in Figure 4b;

(3) With an increase in the longitudinal bar diameter of the concealed column, the bearing capacity of the corroded specimen increased significantly, but this had little effect on the deformation capacity of the specimen, mainly because the final failure of the corroded specimen changed from bending failure to bending shear failure. However, due to the small diameter of the longitudinal bars in specimen SW-9, the deformation capacity of the bending failure was limited, so the deformation capacities of each specimen were relatively similar, as shown in Figure 4c;

(4) With a decrease in the stirrup spacing of the concealed column, the deformation capacity of the corroded specimen increased significantly, but this had little impact on the bearing capacity. The main reason for this was that the decrease in the stirrup spacing

of the concealed column increased the restraint capacity of the edge members, which prevented the premature compression buckling of the longitudinal reinforcement and improved the deformation capacity of the corroded specimen, as shown in Figure 4d;

(5) With an increase in the test axial compression ratio, the bearing capacity of the corroded specimen increased more, but the deformation capacity of corroded specimens shown a trend of first increasing and then decreasing. This was mainly due to the significant second-order effect of the specimen, caused by the increase in the axial compression ratio. Due to the second-order effect, the additional bending moment of the specimen increased. Thus, the rapid decline of the bearing capacity and the sudden failure of the specimen occurred, as shown in Figure 4e.
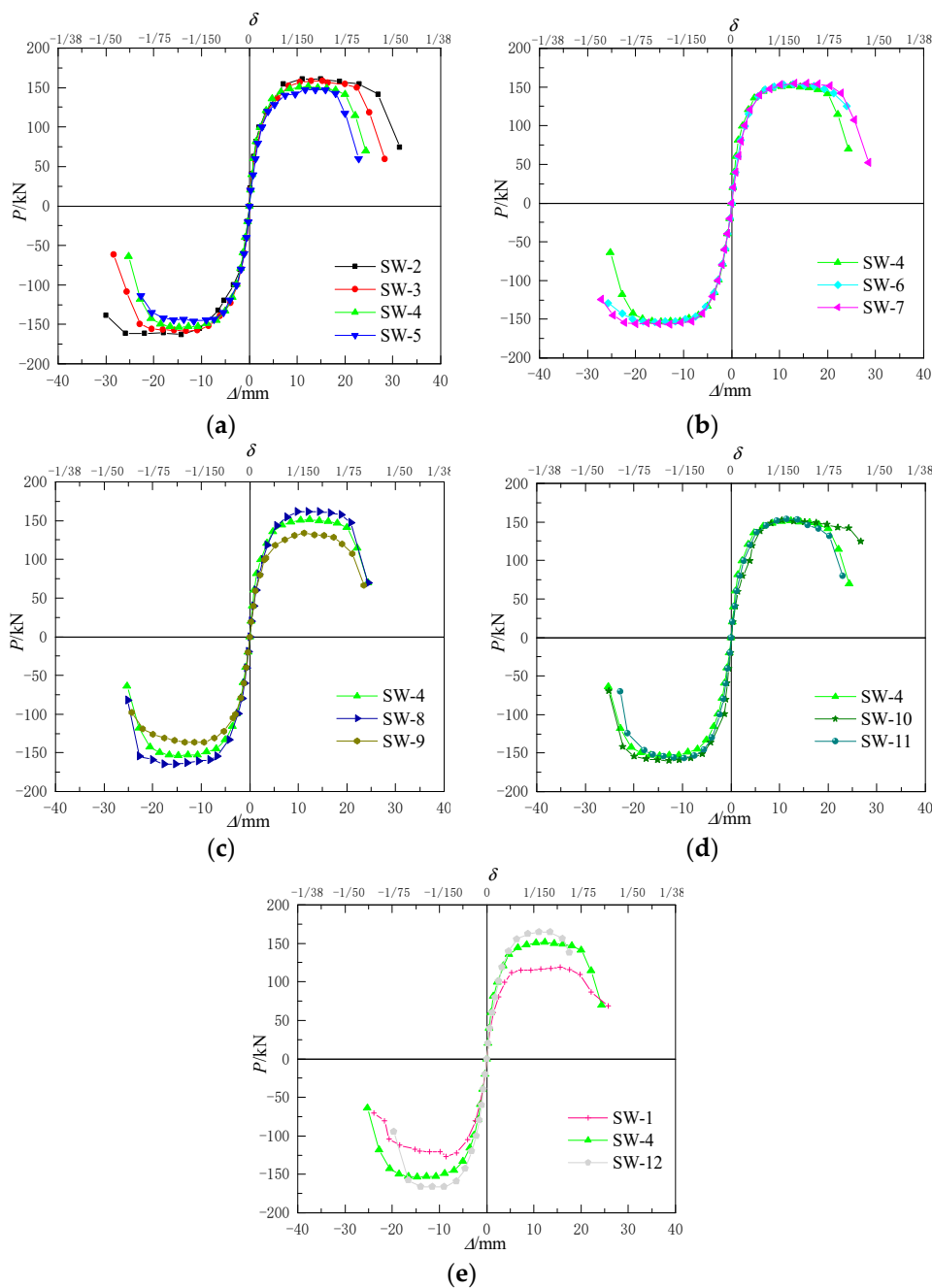
Figure 4. Comparison of the skeleton curves. (**a**) Rust expansion crack width. (**b**) Spacing of the transverse distributed reinforcements. (**c**) Diameter of the longitudinal reinforcement for concealed column. (**d**) Spacing of concealed column stirrups. (**e**) Axial compression ratio.

2.4. The Load and Displacement of Characteristic Point

The new cracks observed with the naked eye in the concealed column were used as the cracking state of the corroded specimen. Furthermore, the yield reference point defined in the loading process was not used as the yield point of this test, and the "energy equivalence method" was used in [16] to determine the yield state. The maximum load of the skeleton curve was used as the peak state. Finally, the peak load when the load drops to 85% was defined as the ultimate failure state. Therefore, the cracking load P_{cr}, yield load P_y, peak load P_m, and failure load P_u of the specimen, as well as the corresponding cracking displacement Δ_{cr}, yield displacement Δ_y, peak displacement Δ_m, and limit displacement Δ_u, could be determined. The load and displacement test values of each characteristic point are shown in Table 3.

Table 3. The value of the characteristic point.

| Specimen No.	P_{cr}/kN	P_y/kN	P_m/kN	P_u/kN	Δ_{cr}/mm	Δ_y/mm	Δ_m/mm	Δ_u/mm
SW-1	80.38	106.25	123.06	104.60	2.48	4.43	12.10	20.10
SW-2	99.91	132.42	161.66	137.41	2.68	5.76	14.56	28.62
SW-3	100.02	131.86	158.65	134.85	2.58	5.22	13.08	23.79
SW-4	99.46	130.92	152.41	129.55	2.57	4.63	13.50	21.32
SW-5	79.68	124.28	146.79	124.77	1.74	4.69	12.68	20.47
SW-6	99.46	132.60	153.59	130.55	2.80	5.12	14.40	24.31
SW-7	90.03	134.29	155.61	132.27	2.70	5.26	14.25	24.89
SW-8	80.00	139.96	162.98	138.53	1.78	5.19	14.80	22.24
SW-9	99.72	114.00	135.17	114.90	3.43	4.60	11.28	21.28
SW-10	79.98	133.50	156.12	132.70	1.72	4.80	11.61	24.30
SW-11	79.80	132.35	155.29	132.00	1.63	4.60	10.54	20.10
SW-12	109.74	142.55	165.50	140.68	2.75	4.74	10.01	17.38

It can be seen from Table 3 that corrosion had a serious impact on the bearing capacity (cracking load, yield load, and peak load) and ductility (cracking displacement, yield displacement, and ultimate displacement) of RC shear wall specimens with a shear span ratio of 2.14. Reducing the spacing of transverse distributed bars had little impact on the bearing capacity of corroded specimens, but it effectively improved the ductility. Moreover, increasing the diameter of the longitudinal reinforcement of concealed columns significantly improved the bearing capacity of corroded specimens, but the ductility of corroded specimens was reduced, and the corroded specimens with the same thickness of protective layer were seriously damaged. In addition, reducing the spacing of stirrups in concealed columns significantly improved the ductility of corroded specimens, but it had little effect on the bearing capacity because the length of the edge-restrained members was so short. Furthermore, the increase in axial compression ratio effectively improved the bearing capacity of corroded specimens, but the second-order effect had a great impact on the deformation of corroded specimens, resulting in the ductility of corroded specimens decreasing. Therefore, when evaluating the seismic performance of corroded shear wall structures, the axial compression ratio of shear wall components should be strictly controlled.

3. Calculation of Characteristic Point Parameters for Intact RC Shear Wall

According to the conclusions of the pseudo-static test on corroded RC shear wall described in Section 2, reinforcement corrosion had a great impact on the seismic performance index of RC shear wall, as shown in Figure 5, and changing the design parameters of RC shear wall can effectively improve the seismic performance of corroded RC shear wall. Therefore, the restoring force model needed to take into account not only the influence of reinforcement corrosion but also the change in the design parameters of corroded RC shear wall. Immediately, the load test data of corroded members were statistically analyzed

to obtain the reduction coefficient of the skeleton curve characteristic point parameters, in terms of corrosion rate. Based on the existing calculation formulas of intact members (considering the change in design parameters) for characteristic point parameters, the corroded members were obtained. These parameters comprehensively took into account the interaction between corroded reinforcement and concrete.
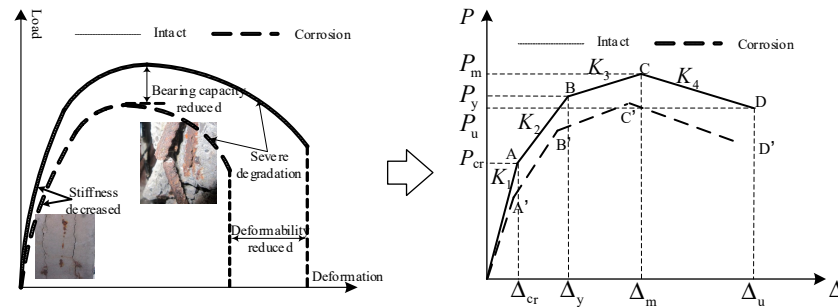
Figure 5. Comparison of skeleton curves for corroded members.

In this study, a four-fold skeleton curve that took into account the descending section was adopted for the intact RC shear wall. It was assumed that the skeleton curves for forward and reverse were the same, as shown in Figure 5. The cracking state of the specimen was determined by observing new cracks in the hidden columns of the wall, and the yield state was determined using the "energy equivalence method". Furthermore, the maximum load on the skeleton curve was used as the peak state. A load drop to 85% was considered as the ultimate failure state. A total of eight parameters needed to be determined, namely, cracking load P_{cr} and cracking displacement Δ_{cr}, yield load P_y and yield displacement Δ_y, peak load P_m and peak displacement Δ_m, and ultimate load P_u and ultimate displacement Δ_u. The corresponding calculation formulas were as follows.

3.1. Calculation of Cracking Load and Displacement

When sliding micro-cracks appeared in the concrete aggregate section in the plastic-hinge area of the wall, the state corresponding to the stable crack development stage of the concrete was defined as the cracking state, as outlined in [17]. Because the RC shear wall was basically in an elastic stage before cracking, its corresponding cracking load P_{cr} and cracking displacement Δ_{cr} could be calculated, approximately, according to the cantilever beam or by fitting regression with a large number of test data. A formula was proposed in [18] which considered the influence of axial pressure P on cracking load. Therefore, the cracking load of the intact shear wall was calculated according to the following formula.

$$P_{cr} = 4\sqrt{f_c'} \left[1 + \frac{P/A_g}{4\sqrt{f_c'}} \right]^{1/2} A_{cv} \tag{1}$$

where A_g is the cross-sectional area of the wall (in^2), A_{cv} is the net area of the wall web (in^2), and f_c' is the axial compressive strength of the cylinder (PSI).

The crack displacement Δ_{cr}' of the RC shear wall was calculated by the cantilever beam crack displacement calculation method in material mechanics described in [19], as follows:

$$\Delta_{cr}' = \frac{P_{cr}H^3}{3E_c I_w} + \mu \frac{P_{cr}H}{G_c A} \tag{2}$$

where H is the height of the shear wall (mm); E_c is the elastic modulus of the concrete (MPa); I_w is the section moment of inertia (mm^4); μ is the non-uniform coefficient of the shear stress distribution (the rectangular section used was $\mu = 1.2$); G_c is the shear modulus of concrete (MPa), where $G_c = 0.4E_c$; and A is the cross-sectional area of the wall (mm^2).

After comparison with the test data in the literature, as shown in Figure 6, the calculated value was smaller than the test value as a whole. The main reason for this was that the internal micro-cracks had been fully developed before the visible cracks appeared on the wall surface. By fitting the discrete points in Figure 6, the calculation formula of cracking displacement Δ_{cr} was modified in Formula (3):

$$\Delta_{cr} = 1.7\Delta_{cr}' \tag{3}$$
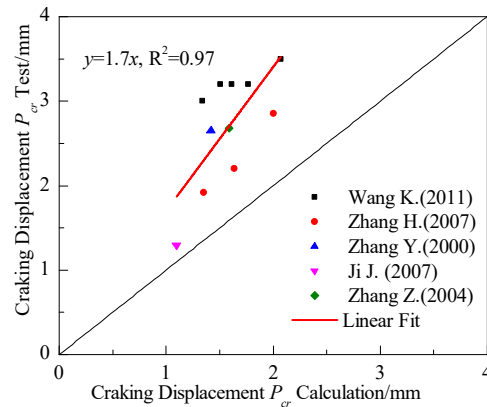
Figure 6. Comparison of calculation of test value [20–24].

3.2. Calculation of Yield Load and Displacement

Since there was no obvious inflection point on the skeleton curve of the shear wall specimen, the yield of the longitudinal bar was generally defined as the yield of the specimen during the test loading process. During data processing, the yield state of the specimen was generally redefined by the equal energy method or the yield moment method, which increased the difficulty of determining the yield point. The yield load P_y was mainly obtained by statistical regression using a large number of test data. The yield displacement Δ_y was mainly derived by calculating the section curvature. In this paper, the formula proposed in [25] was selected to calculate the yield load, as follows:

$$P_y = \frac{P_m}{2.05 - 0.31n + 0.4\lambda_v - 0.34\lambda} \tag{4}$$

where P_m is the peak shear force of the shear wall (kN), n is the axial compression ratio of the shear wall, λ_v is the hooping characteristic value of the edge member, and λ is the shear span ratio of the shear wall.

In addition, the model outlined in Ref. [26] model was selected to calculate the yield displacement of the intact shear wall, as follows:

$$\Delta_y = \frac{1}{3}\frac{\kappa_\phi}{l_w}h_w^2 \tag{5}$$

where $\kappa_\phi = 1.8\varepsilon_y + 0.0045n$, ε_y is the yield strain of the longitudinal reinforcement for the edge member, n is the axial compression ratio of the wall, h_w is the effective height of the wall specimen (mm), and l_w is the length of the wall section (mm).

3.3. Calculation of Peak Load and Displacement

Peak shear force is the load value corresponding to the highest point of the skeleton line, that is, the bearing capacity of the test specimen. Many studies have been carried out on the calculation formula of the bearing capacity for shear walls. These studies primarily used multi-parameter fitting for a large number of test data. In Ref. [27], it was determined that the shear capacity calculation formula of a shear wall, based on 313 shear

wall test data collected in China, can be calculated using a calculation model with the following specifications:

$$P_{\mathrm{m}} = \frac{1}{\lambda - 0.5}\left(1.1912 f_t b_{\mathrm{w}} h_{\mathrm{w}0} + 0.1447 N \frac{A_{\mathrm{w}}}{A}\right) + f_{\mathrm{yh}} h_{\mathrm{w}0} \frac{A_{\mathrm{sh}}}{s_{\mathrm{h}}} \tag{6}$$

where λ is the shear span ratio, f_t is the axial tensile strength of the concrete (MPa), b_{w} is the thickness of the wall web (mm), $h_{\mathrm{w}0}$ is the effective height of the wall section (mm), N is the axial force (N), A is the full cross-sectional area of the wall (mm2), A_{w} is the area of the wall web, f_{yh} is the tensile strength of the horizontally distributed reinforcement (MPa), A_{sh} is the cross-sectional area of the horizontally distributed reinforcement (mm^2), and s_{h} is the spacing of the horizontally distributed reinforcement (mm).

Because the ductility of the high shear wall was relatively good, the calculation formula for the peak displacement was not clearly provided. In this paper, we primarily calculated the peak displacement according to the method outlined in [28], in which the limit strain of the concrete in the constraint area in the calculation formula of limit displacement was replaced by the peak strain of the concrete. Section 2.4 describes this process in greater detail.

3.4. Calculation of Ultimate Load and Displacement

In the process of test loading, the ultimate failure state was designated as the point when the load drops to 85% of the peak load. Therefore, the ultimate shear force P_{u}, corresponding to the limit point on the skeleton curve, was designated as 0.85 P_{m}, and its accuracy and applicability were not repeated here. The ultimate displacement was calculated by the sum of the deformation in the elastic region and the plastic-hinge region of the shear wall in the ultimate state. In Ref. [29], five different ultimate strain models and four plastic-hinge-length models were combined, respectively. By comparing the calculation results of 20 combined calculation models with the test data, it could be seen that a combination of Ref. [30]'s stress–strain model and Ref. [31]'s plastic-hinge-length model was the most accurate of the 20 combined calculation models. Therefore, this combination was used to calculate the ultimate displacement of the shear wall in this paper. The specific algorithm was as follows:

$$\Delta_{\mathrm{u}} = \eta \frac{\varepsilon_{\mathrm{cu}}}{c} l_p H_{\mathrm{w}}\left(1 + \frac{\Delta_s}{\Delta_f}\right) \tag{7}$$

where Δ_f is the displacement caused by bending deformation (mm), Δ_s is the displacement caused by shear deformation (mm), l_p is the height of the plastic-hinge area (mm), H_{w} is the wall height (mm), $\varepsilon_{\mathrm{cu}}$ is the ultimate compressive strain of the concrete restrained by the concealed column, c is the height of the concrete compression area (mm), and η is the correction coefficient.

4. Calculation of Characteristic Point Parameters for Corroded RC Shear Wall

During the corrosion test on the specimen, the width of the rust expansion crack along the longitudinal reinforcement was used to control the corrosion degree of the RC shear wall. However, as there were many factors affecting the width of the rust expansion crack (reinforcement diameter, protective layer thickness, member type, etc.), it was difficult to establish a unified relationship between the width of the rust expansion crack and its age. On the contrary, there was a good time-varying model between the age and the corrosion rate of the reinforcement. At the same time, when the shear span ratio of the RC shear wall involved in this paper was greater than two, the specimens would undergo bending failure or bending shear failure, and the longitudinal reinforcement of the concealed column contributed greatly to its flexural capacity. To sum up, this paper selected the corrosion rate of the longitudinal reinforcement of the concealed column as the corrosion parameter to characterize the corrosion degree of the RC shear walls.

4.1. Calculation of the Characteristic Point Load

It can be seen from the test results that the bearing capacity of the specimens decreased continuously with the increase in the corrosion rate of the embedded column's longitudinal reinforcement. Furthermore, the diameter of the embedded column's longitudinal reinforcements and the axial compression ratio had a greater impact on the bearing capacity of the corroded specimens. On the contrary, the influence of the spacing of the transverse distributed reinforcements and the embedded column stirrups did not have a significant impact on the bearing capacity of the specimens. Therefore, it was assumed in this paper that the reduction factors of the load parameters at characteristic points of the corroded specimens were only related to the mass loss rate η of the embedded column's longitudinal reinforcement, as well as the reinforcement ratio ρ_v of the embedded column's longitudinal reinforcement and the axial compression ratio n. The load reduction coefficient function was defined as $f(\eta, \rho_v, n)$, so the calculation formula of the characteristic point load of the skeleton curve for the corroded RC shear wall was as follows:

$$P_d = f(\eta, \rho_v, n) P_0 \tag{8}$$

where P_0 was the characteristic point load of intact RC shear wall's skeleton curve, which was calculated as above.

The cracking load of the RC specimens was only related to the strength of the concrete and the size of the members, and the corrosion of the reinforcement had little influence on it. Therefore, we did not reduce the cracking load in this study. Setting $f(\eta, \rho_v, n) = k_\eta k_{\rho v} k_n$, where, k_η, $k_{\rho v}$, and k_n were, respectively, the load correction factors of the corroded specimens, including the mass loss rate η of the embedded column's longitudinal reinforcement; the embedded column's longitudinal reinforcement ratio ρ_v; and the axial compression ratio n under single-factor conditions. According to the test data in this paper, the characteristic point loads of corroded RC shear walls were normalized based on the intact RC shear wall specimens with $\eta = 0$, $\rho_v = 4.52\%$, and $n = 0.2$ and the corroded specimens with $\eta = 5.63\%$, $\rho_v = 4.52\%$, and $n = 0.2$. The calculation formulas of the load correction coefficient of each characteristic point were fitted by 1stOpt7.0 software, as follows:

(1)   Yield point:

$$k_\eta = 1 - 0.55\eta \tag{9}$$

$$k_{\rho_v} = 0.776 + 4.82\rho_v. \; (\rho_v > \rho_{\min}) \tag{10}$$

$$k_n = 0.699 + 1.46n. \; (n < n_t) \tag{11}$$

(2)   Peak point:

$$k_\eta = 1 - 1.06\eta \tag{12}$$

$$k_{\rho_v} = 0.799 + 4.42\rho_v. \; (\rho_v > \rho_{\min}) \tag{13}$$

$$k_n = 0.694 + 1.49n. \; (n < n_t) \tag{14}$$

In Equations (10), (11), (13), and (14), $\rho_{\min}$ was the minimum reinforcement ratio of the longitudinal reinforcement for edge restraint members, and n_t was the limit value of the axial compression ratio for the RC shear walls. The characteristic point load values of the 12 corroded RC shear wall specimens involved in this paper were calculated using Equations (9)–(14), respectively. Comparison with the test values is shown in Table 4. The errors of the calculated and experimental values are shown in Figure 7. It can be seen that

the calculated values of the cracking point, yield point, and peak point loads were close to the test values.

Table 4. Comparison of calculated and experimental load values of characteristic points for skeleton curves.

Specimen No.	Cracking Load		Yield Load		Peak Load	
	Test/kN	Calculation/kN	Test/kN	Calculation/kN	Test/kN	Calculation/kN
SW-1	80.38	76.85	106.25	109.23	123.06	125.05
SW-2	99.91	76.87	132.42	120.05	161.66	171.99
SW-3	100.02	76.87	131.86	118.57	158.65	167.91
SW-4	99.46	76.87	130.92	116.33	152.41	161.73
SW-5	79.68	76.87	124.28	114.49	146.79	156.64
SW-6	99.46	76.87	132.6	116.53	153.59	173.91
SW-7	90.03	76.87	134.29	116.41	155.61	195.33
SW-8	80	76.87	139.96	126.42	162.98	175.83
SW-9	99.72	76.87	114	101.76	135.17	142.69
SW-10	79.98	76.87	133.5	114.65	156.12	161.20
SW-11	79.8	76.87	132.35	117.87	155.29	163.13
SW-12	109.74	76.89	142.55	136.60	165.5	204.32
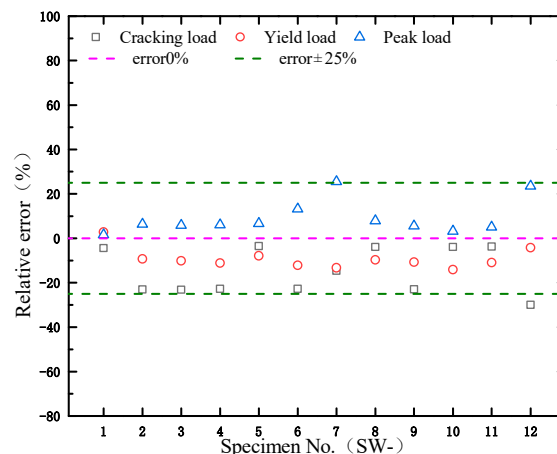
Figure 7. Error diagram of calculated and experimental load values.

4.2. Calculation of Characteristic Point Displacement

It can be seen from the test results that the displacement of the characteristic points on the skeleton curve of the specimen changed greatly due to the corrosion, and the axial compression ratio had a more obvious influence than other design parameters on the displacement of characteristic points for the corroded specimens. Therefore, it was assumed in this paper that the displacement influence coefficient of the characteristic point for the corroded RC shear wall was only related to the mass loss rate η of the embedded column's longitudinal reinforcement and axial compression ratio n. The displacement influence coefficient function was defined as $g(\eta,n)$, so the calculation formula of the characteristic point displacement for the corroded RC shear wall was as follows:

$$\Delta_d = g(\eta,n)\Delta_0 \tag{15}$$

where Δ_0 was the characteristic point displacement of the intact RC shear wall, which was calculated as above.

The cracking displacement of the RC members was only related to the strength of the concrete and the size of the members, and the corrosion of the reinforcement had little influence on it. Therefore, this paper did not consider correcting the cracking displacement. We used the following settings: $g(\eta,n) = l_\eta l_n$, where l_η and l_n are the displacement correction

coefficients of corroded specimens for the mass loss rate η and the axial compression ratio n, respectively. According to the test data in this paper, the characteristic point displacement of the corroded RC shear walls was normalized based on the intact RC shear wall specimens with $\eta = 0$ and $n = 0.2$ and the corroded specimens with $\eta = 5.63\%$ and $n = 0.2$. The calculation formulas of the displacement correction coefficient of each characteristic point were fitted using the 1stOpt software, as follows:

(1) Yield point:

$$l_\eta = 1 - 0.7\eta^{0.5} \tag{16}$$

$$l_n = 0.93 + 0.335n. \ (n < n_t) \tag{17}$$

(2) Peak point:

$$l_\eta = 1 - 0.43\eta^{0.5} \tag{18}$$

$$l_n = 17.6ne^{-6.3n}. \ (n < n_t) \tag{19}$$

(3) Limit point:

$$l_\eta = 1 - \eta^{0.5} \tag{20}$$

$$l_n = 17.5ne^{-6.23n}. \ (n < n_t) \tag{21}$$

In Formulas (17), (19), and (21), n_t was the limit value of the axial compression ratio for the RC shear wall. The characteristic point displacement values of the 12 corroded specimens involved in this paper were calculated according to Equations (16)–(21), respectively. Furthermore, a comparison with the test values is shown in Table 5, and the errors of calculated and experimental values are shown in Figure 8. It can be seen that the calculated values of crack point and peak point displacement were close to the test values; however, there was a significant error in the calculated values of SW-7, SW-8, SW-9, and SW-10, mainly due to the fact that the displacement formula did not adequately consider the influence of changes in the reinforcements in the shear walls. The calculated values of yield point and limit point displacement were about 25% less than the test values, mainly due to the error in the original displacement formula for the intact specimen. In summary, the accuracy of the displacement formula still needs further improvement.
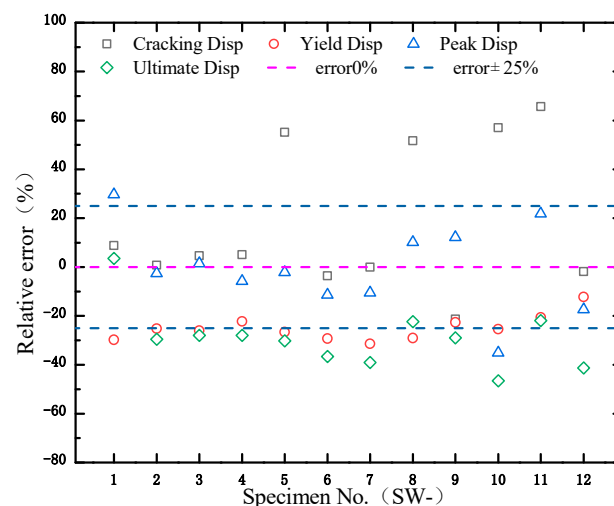
Figure 8. The error diagram of calculated and experimental displacement values.

Table 5. Comparison of calculated and experimental displacement values of characteristic points for skeleton curves.

Specimen No.	Cracking Disp.		Yield Disp.		Peak Disp.		Ultimate Disp.	
	Test/mm	Calculation/mm	Test/mm	Calculation/mm	Test/mm	Calculation/mm	Test/mm	Calculation/mm
SW-1	2.48	2.70	4.43	3.11	12.1	15.69	20.1	20.82
SW-2	2.68	2.70	5.76	4.31	14.56	14.18	28.62	20.15
SW-3	2.58	2.70	5.22	3.86	13.08	13.27	23.79	17.13
SW-4	2.57	2.70	4.63	3.60	13.5	12.73	21.32	15.37
SW-5	1.74	2.70	4.69	3.44	12.68	12.41	20.47	14.30
SW-6	2.8	2.70	5.12	3.62	14.4	12.77	24.31	15.40
SW-7	2.7	2.70	5.26	3.61	14.25	12.75	24.89	15.17
SW-8	1.78	2.70	5.19	3.68	14.8	16.30	22.24	17.26
SW-9	3.43	2.70	4.6	3.56	11.28	12.66	21.28	15.11
SW-10	1.72	2.70	4.8	3.58	11.61	7.54	24.3	12.98
SW-11	1.63	2.70	4.6	3.65	10.54	12.84	20.1	15.70
SW-12	2.75	2.70	4.74	4.16	10.01	8.27	17.38	10.20

5. Conclusions

(1) The corrosion had a great influence on the skeleton curve of the RC shear walls. With an increase in the corrosion degree, the bearing capacity of the specimen decreased, and the deformation capacity worsened. The reduction in the transverse distributed reinforcement and the stirrup spacing of the embedded column had little effect on the bearing capacity of the corroded specimens. However, the bearing capacity of the corroded specimens decreased significantly with a decrease in the diameter of the embedded column's longitudinal reinforcement. With an increase in axial compression ratio, the bearing capacity of the corroded specimens increased. On the contrary, the deformation decreased.

(2) The calculation formula for the characteristic point parameters of the intact RC shear walls was analyzed based on the existing literature, and the calculation formula with the best accuracy was selected as the calculation formula for characteristic point parameters for the intact RC shear walls.

(3) Considering the influence of corrosion on the seismic performance for the test specimens, the characteristic-point reduction coefficient functions, taking into account axial compression ratio, longitudinal reinforcement ratio, and reinforcement corrosion rate, were obtained by fitting. Combined with the calculation formulas of the characteristic points for the intact RC shear walls, the calculation formulas of the characteristic points for the corroded RC shear wall were finally determined. Compared with the test results, it was found that the proposed formula demonstrated good accuracy.

Author Contributions: Conceptualization, Q.Q. and H.C.; methodology, Q.Q.; validation, S.D. and C.Z.; formal analysis, H.C.; investigation, H.C.; resources, C.Z.; data curation, S.D.; writing—original draft preparation, Q.Q.; writing—review and editing, Q.Q.; project administration, C.Z.; funding acquisition, Q.Q. All authors have read and agreed to the published version of the manuscript.

Data Availability Statement: The data presented in this study are available on request from the corresponding author. The data are not publicly available due to privacy policies.

Conflicts of Interest: The authors declare that they have no conflicts of interest.

References

1. Verstrynge, E.; Van Steen, C.; Vandecruys, E.; Wevers, M. Steel corrosion damage monitoring in reinforced concrete structures with the acoustic emission technique: A review. *Constr. Build. Mater.* **2022**, *349*, 128732. [CrossRef]
2. Zhou, Y.; Zheng, S.; Chen, L.; Long, L.; Dong, L.; Zheng, J. Experimental and analytical investigations into the seismic behavior and resistance of corroded reinforced concrete walls. *Eng. Struct.* **2021**, *238*, 112154. [CrossRef]
3. Mahadik, S.; Bhagat, S.R. Experimental and numerical study of behavior of RC shear wall using concealed stiffeners. *Jordan J. Civ. Eng.* **2022**, *16*, 193–210. [CrossRef]
4. Mahadik, S.; Bhagat, S.R.; Gunaware, P.D.; Patil, V.N. Experimental and numerical study of the behavior of RC shear wall with opening using concealed stiffeners. *Jordan J. Civ. Eng.* **2023**, *17*, 203–218. [CrossRef]
5. Yamakawa, T.; Iraha, S.; Tamaki, Y.; Matsunaga, T.; Biwada, A. An experimental study on damage affecting aseismatic behavior of structural walls under chloride attack environment in the semitropical region. *Univ. Ryukyus Repos.* **1993**, *46*, 115–130.
6. Zhuang, Y. *Life-Cycle Seismic Performance Evaluation for Deteriorating RC Shear Walls*; National Taiwan University of Science and Technology: Taipei, Taiwan, 2012.
7. Shansuo, Z.; Qing, Q.; Wei, Y. Experimental research on the seismic behaviors of squat RC shear walls under offshore atmospheric environment. *J. Harbin Inst. Technol.* **2015**, *47*, 64–69.
8. Zheng, Y.; Zheng, S.S.; Yang, L.; Dong, L.G.; Ruan, S.; Ming, M. Experimental study on the seismic behavior of corroded reinforced concrete walls in an artificial climate corrosion environment. *Eng. Struct.* **2022**, *252*, 113469. [CrossRef]
9. Shen, D.; Yang, Q.; Huang, C.; Cui, Z.; Zhang, J. Tests on seismic performance of corroded reinforced concrete shear walls repaired with basalt fiber-reinforced polymers. *Constr. Build. Mater.* **2019**, *209*, 508–521. [CrossRef]

10. Li, M.; Shen, D.; Yang, Q.; Cao, X.; Huang, C.; Cui, Z.; Qi, Y. Effect of reinforcement corrosion on the seismic performance of reinforced concrete shear walls. *Constr. Build. Mater.* **2023**, *377*, 130977. [CrossRef]

11. Yang, L.; Zheng, S.S.; Zheng, Y.; Dong, L.G.; Wu, H.L. Experimental investigation and numerical modelling of the seismic performance of corroded T-shaped reinforced concrete shear walls. *Eng. Struct.* **2023**, *283*, 115930. [CrossRef]

12. Liu, X.H.; Zheng, S.S.; Wang, W.; Liu, H.; Zheng, Y.; Zheng, H. Experimental study on the seismic behaviour of a corroded T-shaped RC shear wall. *J. Build. Eng.* **2023**, *76*, 107071. [CrossRef]

13. *JGJ3-2010*; Technical Specification for Concrete Structures of Tall Buiding. China Architecture & Building Press: Beijing, China, 2010.

14. Qin, Q.; Zheng, S.; Ding, S. Experimental Study on Aseismic Behavior of Short-Pier RC Shear Walls in Salt-Fog Environment. *Eng. Mech.* **2020**, *37*, 79–92.

15. *JGJ/T101-2015*; Specification for Seismic Test of Buildings. China Architecture & Building Press: Beijing, China, 2015.

16. Zhu, B. *Structural Seismic Test*; Seismological Press: Beijing, China, 1989; pp. 128–130.

17. Yan, L.; Liang, X.; Xu, J.; Wang, H. Research on calculation method of deformation capacity of reinforced concrete shear wall. *Eng. Mech.* **2014**, *31*, 92–99.

18. Wallace, J.W. Modelling Issues for Tall Reinforced Concrete Core Wall Buildings. *Struct. Des. Tall Spec. Build.* **2007**, *16*, 615–632. [CrossRef]

19. Shi, Q.; Liang, X. *Structural Design of High-Rise Buildings*, 2nd ed.; Science Press: Beijing, China, 2012.

20. Wang, K. *Experimental Researches on Restoring Force Model of Reinforced Concrete Shear Wall Based on Damage*; Xi'an University of Architecture and Technology: Xi'an, China, 2011.

21. Zhang, H. *Study on the Performance-Based Seismic Design Method for Shear Wall Structures*; Tongji University: Shanghai, China, 2007.

22. Zhang, Y.; Wang, Z. Seismic Behavior of Reinforced Concrete Shear Walls Subjected to High Axial Loading. *ACI Struct. J.* **2000**, *97*, 739–749.

23. Ji-Dong, C.; Xiao-Lei, H.; Wan, Y.; Wei-Chen, L. Study on comparative experiments of shear walls without boundary elements. *Build. Sci.* **2007**, *23*, 41–45.

24. Zhang, Z.; Zhou, K. Experimental study on seismic behavior of high-performance concrete shear walls with various aspect ratios. *Struct. Eng.* **2004**, *20*, 62–68. [CrossRef]

25. Zhang, S.; Lv, X.; Zhang, H. Experimental and analytical studies on resilience models of RC shear walls. *J. Shenyang Jianzhu Univ. (Natl. Sci.)* **2009**, *4*, 643–649.

26. Tjhin, T.N.; Aschheim, M.A.; Wallace, J.W. Yield Displacement Estimates for Displacement-based Seismic Design of Ductile Reinforced Concrete Structural Wall Buildings. In Proceedings of the 13th World Conference on Earthquake Engineering, Vancouver, BC, Canada, 1–6 August 2004.

27. Liang, X. *Theory and Method of Structural Seismic Performance Design*; Science Press: Beijing, China, 2011.

28. Kou, J.; Liang, X.; Deng, M. Experimental and theoretical study of restoring force model of fiber reinforced concrete shear walls. *China Civ. Eng. J.* **2013**, *10*, 58–70.

29. Lu, Y.; Huang, L. Experimental data-based calculation method for ultimate displacement of flexure dominated RC walls with concealed columns. *J. Build. Struct.* **2014**, *2*, 11–20.

30. Saatcioglu, M.; Razvi, S.R. Strength and Ductility of Confined Concrete. *J. Struct. Eng.* **1992**, *118*, 1590–1607. [CrossRef]

31. Paulay, T.; Priestley, M.J.N. Stability of Ductile Structural Walls. *ACI Struct. J.* **1993**, *90*, 385–392.